Charge transport in Si nanocrystal/SiO2 superlattices

S. Gutsch, J. Laube, A. M. Hartel, D. Hiller, N. Zakharov, P. Werner, and M. Zacharias

Citation: Journal of Applied Physics **113**, 133703 (2013); doi: 10.1063/1.4798395
View online: http://dx.doi.org/10.1063/1.4798395
View Table of Contents: http://scitation.aip.org/content/aip/journal/jap/113/13?ver=pdfcov
Published by the AIP Publishing

Charge transport in Si nanocrystal/SiO_2 superlattices

S. Gutsch,[1] J. Laube,[1] A. M. Hartel,[1] D. Hiller,[1] N. Zakharov,[2] P. Werner,[2] and M. Zacharias[1]
[1]*IMTEK, Faculty of Engineering, Albert-Ludwigs-University Freiburg, Georges-Köhler-Allee 103, 79110 Freiburg, Germany*
[2]*Max-Planck-Institute of Microstructure Physics, Weinberg 2, 06120 Halle, Germany*

(Received 6 February 2013; accepted 13 March 2013; published online 1 April 2013; publisher error corrected 8 April 2013)

Size-controlled silicon nanocrystals in silicon oxynitride matrix were prepared using plasma-enhanced chemical vapor deposition following the superlattice approach. A combination of current transport and charge trapping studies is carried out on a number of samples with varied structural configuration. We demonstrate that at low electric fields, trapping of injected carriers dominates, if the coupling between the silicon nanocrystals is strong. In contrast, we show that at higher electric fields, the charge distribution within the films is essentially governed by charge separation within the superlattice. This effect can be well explained by a two-step electric field ionization of silicon nanocrystals that proceeds via defect-assisted band-to-band tunneling of silicon valence electrons to the conduction band and is mediated by silicon surface dangling bonds. The defects are dominating the charge transport even if the defect density is reduced to a minimum by efficient hydrogen passivation. © *2013 American Institute of Physics*. [http://dx.doi.org/10.1063/1.4798395]

I. INTRODUCTION

Since the discovery of visible light emission from silicon,[1,2] many optoelectronic applications such as light emitting diodes,[3,4] lasers[5,6] and tandem solar cells[7] have been envisioned based on the abundant, non-toxic, and well known material. It has been shown that the optical bandgap of solid-state crystalized silicon nanocrystals (SiNC) embedded in SiO_2 can be tuned between 1.3 and 1.7 eV.[8,9] Size-control is achieved via the superlattice (SL) approach,[8] where thin silicon rich oxide (SRO) layers are separated by thin SiO_2 diffusion barriers. In a subsequent high temperature annealing, phase separation of the SRO leads to the formation of SiNCs embedded in SiO_2 matrix. Based on this approach, SiNCs embedded in a dielectric matrix have been proposed for use in third generation photovoltaic (PV) devices.[7] Due to the high bandgap of SiO_2 (~9 eV), different host materials such as Si_3N_4 and SiC could act as possible alternative matrix materials. However, SiO_2 is still a competitive choice due to the comparably low defect density, the excellent interface properties to Si,[10,11] and the preservation of its amorphous state even in the high temperature annealing needed for the crystallization of SiNCs. Apparently, due to the large band offsets between Si and SiO_2, the main challenge associated with the SiO_2 matrix material is charge transport. Theoretical considerations have shown that strong SiNC-SiNC coupling and hence charge transport is only achievable, if the SiNCs have tight size tolerances and are almost in intimate contact with each other.[12–15] In a recent review on transport properties of SiNC ensembles, it was shown that a percolation threshold exists for a bulk film conductivity at about 40% excess silicon.[16] However, bulk films with such a high silicon content have a large SiNC size and shape dispersion and control of the bandgap can hardly be achieved. Therefore, the SL approach seems mandatory for solar cell devices based on SiNCs. Surprisingly, detailed studies on transport in such Si/SiO_2 multilayers are rarely found.[17–19]

II. EXPERIMENTAL DETAILS

A. Sample preparation

In the present work, lowly doped n-type 4 in. (100)-silicon wafers (phosphorus doped, conductivity 5–20 Ω cm) were used as a substrate material. All samples were cleaned in Caro's acid for 10 min followed by a 15 s etch in diluted hydrofluoric acid (HF) to remove the chemically formed SiO_2. Immediately after the HF dip, the samples were loaded into the plasma-enhanced chemical vapor deposition (PECVD) chamber. Alternating layers of SiO_2 and silicon rich silicon oxynitride (SRON) were deposited according to the data in Table I. It should be noted that the SRON layer contains around 10 at. % of nitrogen. Further data concerning the PECVD process can be found elsewhere.[20] The samples were capped with a 10 nm SiO_2 layer that serves as annealing protection. Subsequently, all samples were annealed at 1150 °C in purified N_2 atmosphere to induce precipitation and crystallization of the SiNCs followed by a hydrogen passivation in a pure molecular hydrogen atmosphere for 1 h at 500 °C. Aluminum dots were patterned thereafter by conventional lift-off technology. In order to achieve a good front contact, the SiO_2 capping layer was etched in highly diluted buffered HF prior to aluminum evaporation. The wafer front side was then protected by a standard photoresist followed by backside metallization using aluminum sputtering. A schematic of the final device structure is shown in Fig. 1(e). Two sets of samples were studied within this work. In the first set of samples named S1 to S8 (cf. Table I), the transport and charge trapping properties of SiNC/SiO_2 SLs were studied as a function of SiO_2 barrier thickness, number of bilayers, and the stoichiometry of the SRON layer. A second set of samples H1 to H4 (cf. Table II) were prepared as listed in Table II in order to evaluate the influence of hydrogen passivation. H1 and H2 consist of the same layer parameters as samples S3 to S6, but with 22 bilayers to achieve a total layer thickness of around

TABLE I. List of samples investigated in this work by means of I-V and C-V measurements.

Name	SL structure	d_{nom} (nm)	d_{TEM} (nm)	d_{SRON} (nm)	d_{SiO2} (nm)
S1	5 × (4 nm SiO_2/3.5 nm $SiO_{0.93}$)	37.5	39.7 ± 1	3.6 ± 0.2	3.9 ± 0.2
S2	5 × (2 nm SiO_2/3.5 nm $SiO_{0.93}$)	27.5	28.7 ± 1	3.2 ± 0.3	2.3 ± 0.3
S3	5 × (1 nm SiO_2/3.5 nm $SiO_{0.93}$)	22.5	21.9 ± 1	2.4 ± 0.4	2.0 ± 0.3
S4	10 × (1 nm SiO_2/3.5 nm $SiO_{0.93}$)	45.0	…	…	…
S5	20 × (1 nm SiO_2/3.5 nm $SiO_{0.93}$)	90.0	86.2 ± 1	2.1 ± 0.3	2.0 ± 0.3
S6	30 × (1 nm SiO_2/3.5 nm $SiO_{0.93}$)	130.0	…	…	…
S7	5 × (1 nm SiO_2/3.5 nm $SiO_{0.85}$)	22.5	…	…	…
S8	5 × (1 nm SiO_2/3.5 nm $SiO_{0.64}$)	22.5	…	…	…

100 nm. H3 and H4 consist of a SL that is sandwiched between two 10 nm SiO_2 tunneling barriers that should efficiently prevent charge injection from the device contacts at low electric fields. With the sample series H, the effect of hydrogen passivation on the internal charge flow can be disentangled from charge injection at the contacts.

The cross-sectional bright field transmission electron microscope (TEM) images were taken under Fresnel defocus conditions[21] using a Jeol JEM 4010 electron microscope operated at 400 kV. The specimens were prepared by mechanical thinning followed by Ar^+-ion milling.

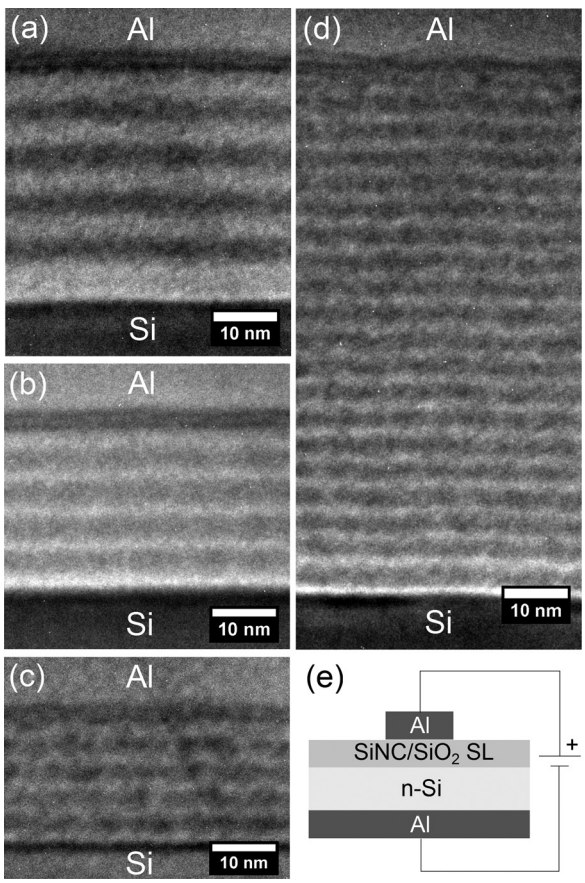

FIG. 1. Underfocus TEM images of samples S1 with a 4 nm SiO_2 barrier (a), S2 with a 2 nm SiO_2 barrier (b), with 1 nm SiO_2 barrier for 5 bilayers, sample S3 (c), and 20 bilayers, sample S5 (d). The final device schematic is also shown (e). In this bright field TEM mode, the silicon rich layers appear in dark, whereas the SiO_2 layers appear bright.

B. Electrical characterization

Electrical characterization was carried out using an Agilent B1500A device analyzer equipped with a multifrequency and a high resolution measurement unit. We define a positive voltage to be applied to the aluminum gate of the device structure. Current-voltage (I-V) measurements have been performed in a slow sweep regime if not stated otherwise. It is reasonable to use a constant change of electric field with time, i.e., $dE/dt = const$ to ensure identical measurement conditions for different sample thicknesses. A sweep rate of around 860 kV m^{-1} s^{-1} turned out to be sufficient to minimize transient effects due to charging and dielectric relaxation.[22–24] Current density versus electric field (J-E) plots were obtained by dividing the measured current by the device area and the gate voltage by the nominal thickness of the layer stack, respectively. Carrier trapping effects were studied in a single pulse capacitance voltage (C-V) mode. First a voltage was applied to the gate and hold for 5 s, if not stated otherwise, immediately followed by a fast C-V sweep in a narrow voltage range around the previously determined flatband voltage. In this way, the C-V curve can be taken in less than 1 s so that slower detrapping and mobile charge effects can be measured by means of a flatband voltage shift ΔV_{FB}. In order to correct for the effect of the dielectric stack thickness and to make ΔV_{FB} comparable between different samples, an effective net mobile charge has been calculated by the well-known expression[25,26] $\bar{Q}_{eff} = -\bar{C}_{ox}\Delta V_{FB}/q$. Here, q is the electric charge and $\bar{C}_{ox}$ is the oxide capacitance per unit area of the device in accumulation that has been corrected for the effect of series resistance. All C-V measurements were carried out at a frequency of 300 kHz.

Please note that measurements with the Si substrate in accumulation were performed in dark, whereas otherwise the measurements were done under microscope illumination

TABLE II. List of samples to study the effect of hydrogen passivation on the trapping and transport properties.

Name	Sample structure	H_2?	d_{nom} (nm)
H1	22 × (1 nm SiO_2/3.5 nm $SiO_{0.93}$)	Yes	99.0
H2	22 × (1 nm SiO_2/3.5 nm $SiO_{0.93}$)	No	99.0
H3	10 nm SiO_2 + 18 × (1 nm SiO_2/3.5 nm $SiO_{0.93}$) + 10 nm SiO_2	Yes	101.0
H4	10 nm SiO_2 + 18 × (1 nm SiO_2/3.5 nm $SiO_{0.93}$) + 10 nm SiO_2	No	101.0

light to supply sufficient minority carriers for the build-up of the inversion layer underneath the gate. It should be noted that measurements in accumulation do not change, when performed under illuminated conditions.

III. RESULTS

A. Structural characterization

The total layer thickness for samples S1 to S3 and S5 was measured at focus condition in the TEM as indicated in Table I. Since the individual sublayers cannot be resolved in standard bright field TEM due to the low contrast between SRON and SiO_2 layers, underfocus images were taken to reveal the stacking of the SL. Figs. 1(a)–1(c) display a series of TEM images of samples S1 to S3, where the SiO_2 barrier thickness is decreased from 4 nm to 2 nm to 1 nm, respectively. In addition, we show in Fig. 1(d) the TEM image of sample S5 which is a 20 bilayer sample with a 1 nm SiO_2 barrier. The layered SL structure is clearly visible for all samples down 1 nm SiO_2 barrier. By integrating the image intensity along the layer growth direction, the individual layer thicknesses were determined[8,21] and are listed in Table I. The SRON layer thicknesses should be constant for all samples. However, this is not the case as the SiO_2 layer thickness is decreased. In contrast the SiO_2 barrier appears larger than expected, but the total stack thickness is in good agreement with the nominal thickness. Hence, we conclude that the SiO_2 barrier layers for S3 and S5 are in the range of 1 nm. When looking at Fig. 1(a), one notices that the first SiO_2 layer between the Si substrate and the first SiNC layer is about 50% larger than intended. We recently demonstrated that this undesirable effect is possibly due to a parasitic oxidation of the Si substrate that is inherent to the here used PECVD process.[27] On the other hand, the aluminum gate appears to be in direct contact with the topmost SiNC layer for all samples studied by TEM as was intended in the fabrication process described above. Nevertheless, to have more confidence on the formation of a good top contact, we studied the stack capacitance as a function of the HF etching time (not shown here). It was observed that the capacitance first decreases continuously and then finally changes very slowly, when the topmost SiNC layer is reached. In fact, the annealed SRON layer seems to act as a good etch stop for the diluted HF due to the high amount of crystalline Si and possibly also due to the presence of nitrogen in the SRON layer. In addition, the I-V characteristics are unaffected even after slightly under- and over-etching the 10 nm SiO_2 capping.

B. Effect of SiO_2 barrier layer thickness

In Fig. 2(a), the J-E characteristics are presented for different SiO_2 barrier thicknesses and a single 50 nm thick SiO_2 layer that serves as a reference sample. When the SiO_2 barrier is decreased, we clearly observe that the onset of a measurable current shifts towards lower electric fields. For 4 nm, the current density is very similar to the reference SiO_2 and can be fitted well with a standard Fowler-Nordheim expression indicating that high field injection into the SiO_2 conduction band dominates for these barriers. Decreasing the barrier to

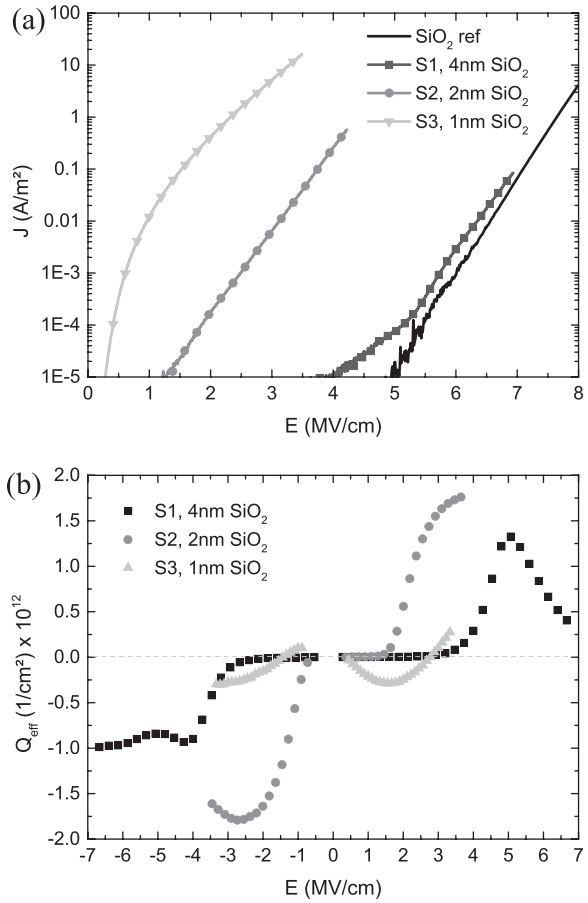

FIG. 2. Current density (a) and effectively trapped charge (b) as a function of applied electric field for samples S1 to S3, where the SiO_2 barrier is varied from 4 nm down to 1 nm.

2 nm and further down to 1 nm leads to a current increase by orders of magnitude as compared to the 4 nm barrier. The strong effect can be understood by the coupling enhancement between adjacent SiNCs in vertical direction enabling direct tunneling of charge carriers. It experimentally demonstrates the necessity of ultrathin barriers to achieve charge transport if using SiO_2 as barrier material.[12–15] In Fig. 2(b), the extracted mobile charge $\bar{Q}_{eff}$ is plotted versus the applied electric field for S1 to S3 (i.e., the samples with varying SiO_2 interlayer thickness). In case of 2 nm and 4 nm SiO_2 barriers, a net positive charge is observed in the dielectric multilayer for positive bias, whereas a net negative charge is observed for negative bias. For these two samples, no net effect of charges that have tunneled from the Si substrate can be observed. Basically, this can be explained by the increased thickness of the first tunneling oxide between the Si substrate and the multilayer as observed by TEM. While the negative charge at negative bias could be associated with electrons from the aluminum gate, it seems unlikely that holes are injected from the gate contact at positive bias. Instead, from the charging pattern described above, a charge separation mechanism can be inferred that will be discussed later. In contrast, the 1 nm SiO_2 barrier sample shows the opposite behavior at low electric fields, viz., negative charging at low positive bias and positive charging at low negative bias, but a similar tendency as samples S1 and S2 at electric fields above

1.5 MV/cm. It can be argued at this point that the negative charge at positive bias and low electric fields is a result of electrons injected by direct tunneling from the Si substrate, while the positive charge at small negative bias may indicate the presence of holes that have tunneled into the multilayer from the inversion layer of the Si substrate. Please note that the absence of electron and hole tunneling from the Si substrate for samples S1 and S2 is most likely linked to the increased thickness of the first SiO_2 tunneling barrier, as observed in the TEM (cf. Figs. 1(a) and 1(b)). This might also affect the J-E characteristics and a more detailed study is needed to clarify the effect of the SiO_2 interlayer barrier.

C. Effect of number of bilayers

As shown in the above Figs. 1(c) and 1(d), a 1 nm SiO_2 barrier is sufficient to preserve the SL structure without dominant SiNC coalescence, i.e., layer intermixing. Thus, it is useful to study the possible contact influence on the observed J-E behavior. This can be achieved by changing the length of the active layer between the two contacts.[25] In a SL, this is easily realized by depositing different number of bilayers. Fig. 3(a) displays the J-E characteristics of samples S3 to S6, where the number of bilayers is increased up to 30. Similar J-E traces are observed indicating that the carrier injection at the contacts plays only a minor role for these samples and that the SL volume dominates the J-E characteristic. At low electric fields, an increasing number of bilayers leads to a damping of the current density rise, whereas at high electric fields the opposite trend is clearly visible. This can be understood, when the charging is considered as presented in Fig. 3(b). At low electric fields, the injected negative charge creates an electric field that is opposed to the applied field at the injection contact, resulting in a space-charge-limited current (cf. Fig. 6(a)). At high electric fields however, the measured negative charge decreases and even positive charging occurs for all samples with more than 5 bilayers. At this condition, the electric field in the contact region is increased so that the device is in a self-biasing region causing a current density rise (cf. Fig. 6(b)).

D. Effect of SRON stoichiometry

Figs. 4(a) and 4(b) display the current and trapping characteristics as a function of SRON stoichiometry. It is observed that the current density is increased, whereas charge trapping effects are decreased as the Si excess in the films is raised. The higher current is expected, since an increased Si excess should lead to a higher SiNC areal density and possibly larger SiNCs such that the electronic coupling between adjacent SiNCs is enhanced. Furthermore, it appears that the decrease in charging may be linked to the enhanced conductivity of the films due to the lower time limit to measure the flatband voltage by means of the C-V sweep. Hence, stored charges may escape the SL within a shorter time and therefore do not contribute to the measured flatband voltage shift.

E. Effect of hydrogen passivation

The electrical analysis of the second sample set H is presented in Fig. 5. Here, the influence of the hydrogen passivation treatment is investigated and it is obvious that the hydrogen passivation decreases the conductivity of the SL (samples H1 and H2) by around one to two orders of magnitude over the whole range of applied electric fields. This is corroborated by a larger charging amplitude for the passivated sample H1 and could be understood by considering the increased current density as discussed in the previous paragraph. The two samples with current blocking layers (H3 and H4) show a small current density up to electric fields of about 2.5 MV/cm, where a steep current density rise sets in for both samples. By using different sweep velocities, one sees in Fig. 5(a) that the current below 2.5 MV/cm is transient and tends to zero at long timescales as demonstrated in the inset of Fig. 5(a). At such a low electric field, no current should be able to pass the 10 nm SiO_2 barriers. Therefore, it can be concluded that the current stems from internal charge transfer within the embedded SL that induces a current in the external circuit according to the Shockley-Ramo theorem.[28–30] This conclusion is supported by the observation of charging (see Fig. 5(b)) that shows a net positive effect at low electric fields and saturation at higher electric fields. Hydrogen passivation clearly delays the charging onset and decreases the magnitude of the charging effects. The current density at electric fields exceeding 2.5 MV/cm has to be ascribed to Fowler-Nordheim tunneling by injection of electrons into the SiO_2 barrier layer. This comparably low onset can be explained by a

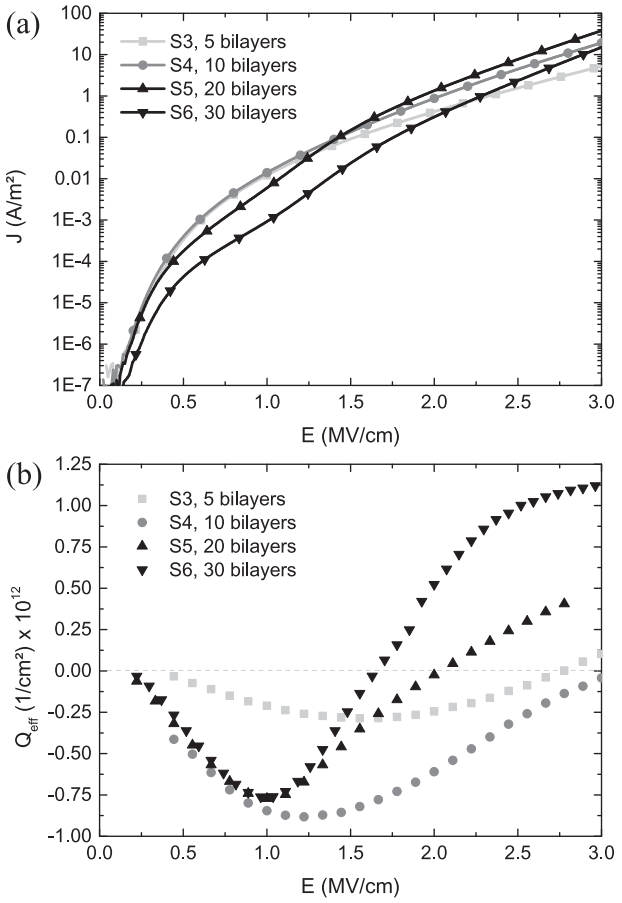

FIG. 3. Current density (a) and effectively trapped charge (b) as a function of applied electric field for samples S3 to S6, where the number of bilayers was changed from 5 to 30. The bias hold time was 60 s in this case.

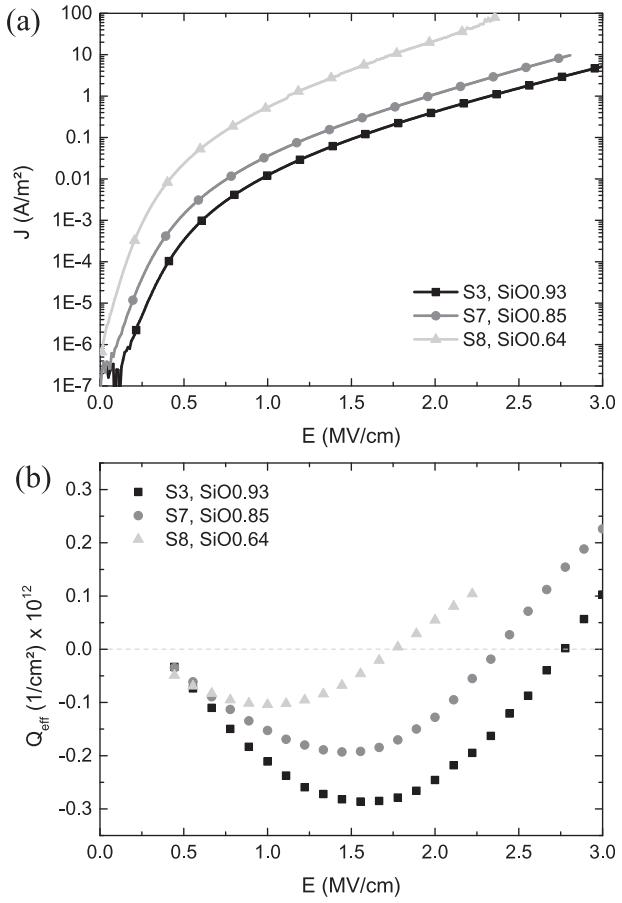

FIG. 4. Current density (a) and effectively trapped charge (b) as a function of applied electric field for samples S3, S7, and S8, where the SRON stoichiometry was changed from $SiO_{0.93}$ down to $SiO_{0.64}$.

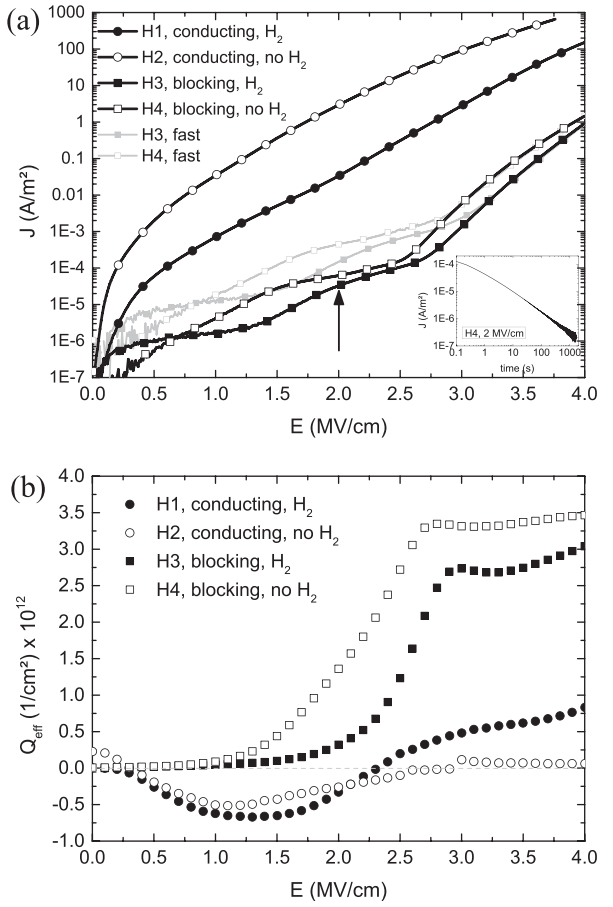

FIG. 5. Current density (a) and effectively trapped charge (b) as a function of applied electric field for samples H1 to H4, where the effect of hydrogen passivation was studied. Here, H3 (■) and H4 (□) are SLs sandwiched between two current blocking SiO_2 layers. Filled symbols (●■) represent samples with a hydrogen passivation, whereas open symbols (○□) represent the samples without hydrogen passivation. In the fast sweep in (a), a sweep rate of 0.5 MV m^{-1} s^{-1} was used. The inset in (a) shows the step response of the current density for sample H4 at an electric field of 2 MV/cm.

charge separation that effectively reduces the potential drop across the SL and significantly increases the potential drop across the buffer and capping layer as shown in Fig. 6(e).

IV. DISCUSSION

A. Transport mechanism

Charge transport properties in conducting SiNC/SiO_2 SLs are commonly attributed to a direct tunneling mechanism.[18,19,31] Hopping conduction models as introduced by Miller and Abrahams[32] require ohmic behavior, i.e., a linear electric field dependence. The electric field dependence of the tunneling transmission coefficient for direct tunneling is generally weak. But then it has to be realized that the direct tunneling currents strongly depend on the contact properties on both sides of the tunneling oxide.[33–35] More precisely, that is the availability of carriers on one side of the barrier and a free density of states on the other side.[36,37] In case of dot-to-dot tunneling, the nature of the wavefunction becomes very important. However, its calculation is a challenging task in case of Si nanostructures.[38] Moreover, the application of strong electric fields leads to a distortion of wavefunctions beyond the applicability of pertubation theory and electronic transitions to states of higher energy will become important. Due to the absence of a suitable model that predicts the J-E characteristics of nanocrystalline composite materials as studied in this work, a Poole-Frenkel fit is often employed.[39–42] Here, $J \propto E \exp(a\sqrt{E}/\varepsilon_r)$ usually describes the J-E characteristics in a small range of electric fields. However, the fitting parameters cast doubts on the suitability of the model.[43] The reason may be the prerequisite of the Poole-Frenkel effect that an electron is released from a neutral trap and the ionized carrier mobility is field-independent.[44] Anyway, using a simple argument, we can rule out the plain application of the Poole-Frenkel effect as a dominating mechanism in our SL structures. The slope of a Poole-Frenkel plot, $\log(J)$ vs. $\sqrt{E}$ is proportional to $1/\varepsilon_r$. Increasing the average dielectric constant should hence decrease the slope of the J-E characteristics. This is in clear disagreement with Fig. 4(a), where J-E characteristics of different Si excess concentrations are plotted. Increasing the Si content in the films also increases the relative dielectric constant ε_r (here from 4.3 to 4.6 as determined from the C-V measurements).

The intrinsically low carrier concentration in SiNC films leads to the observation of trapping effects as shown in the present work as well (cf. Fig. 3(a)). Hence, the space-charge-limited current model was used to interpret the I-V characteristics of SiNC films.[16,45,46] In this model, the current density

behaves as $J \propto V^m$ and the exponent m is a parameter that describes an exponential trap distribution below the mobility edge.[47,48] In the former works, m was determined to be in the range between 2 and 5, whereas our samples yield values between 4 and 8 in the low field range. Please note that the fit quality is questionable. In particular, the average exponent m is decreased when the number of bilayers is increased, whereas the formation of a space-charge is clearly evidenced as shown in Fig. 3(b). Obviously, the current becomes limited by the injected space-charge for thicker films, hence masking the intrinsic conduction mechanism.

A puzzling issue towards further understanding the charge transport is the appearance of a positive injected charge at positive applied bias at electric fields exceeding about 1 MV/cm (cf. Fig. 3(b)), whereas the saturation of the injected electron density is rather expected. In addition, the charging behavior of films with larger barrier thickness (S1 and S2) cannot be explained based on carrier injection from the Al gate or the n-type Si substrate. The creation of holes in SiNC thin films as a result of a positive voltage applied to the gate has been observed by other groups as well.[49,50] The results have been interpreted previously considering band-to-band tunneling that results in the creation of immobile holes[49] and electric field ionization of thermally generated free carriers within the SiNCs.[50] The latter explanation can be excluded for our samples since the effect occurs at comparably low electric fields. In addition, the carrier generation rate at room temperature is most likely not sufficient to have such a strong impact to compensate the effect of the injected charges. The stored electron charge in sample S6 is around $1 \times 10^{12}\,\mathrm{cm}^{-2}$ yielding a lower limit of injected charges in the order of $1 \times 10^{16}\,\mathrm{cm}^{-3}$. In comparison, the room temperature intrinsic carrier density in Si is in the order of $1 \times 10^{10}\,\mathrm{cm}^{-3}$ and can be seen as an upper limit due to the bandgap increase and density of states decrease as a consequence of quantum confinement. In the following, the likeliness of band-to-band tunneling is considered. The SL structure used in this work allows the estimation of the potential drop per bilayer, i.e., the average potential drop between adjacent SiNCs. Considering the samples with just 1 nm barrier, the appearance of holes starts at about 1 MV/cm, which corresponds to a potential drop of roughly 0.45 V per bilayer. This seems quite low to allow for band-to-band tunneling between adjacent SiNCs. The band-bending caused by the internal charge distribution within the SL structures based on the experimental results is summarized in Fig. 6. At low positive applied bias, electron injection from the Si substrate dominates and creates a space-charge region (Fig. 6(a)), whereas at higher bias, charge separation governs the charging behavior (Fig. 6(b)). At a low negative bias, electrons are injected from the metal gate and holes from the inversion layer of the Si substrate (Fig. 6(c)). Without further proof, the internal charge generation and separation should not depend on the contacts and hence should be independent of gate polarization. Thus, one may expect a similar process for highly negative bias leading to the band diagram of Fig. 6(d). Please note that the appearance of a high density of holes and electrons in some regions of the device may lead to recombination and electroluminescence, when the two species are spatially correlated in-plane. Since the

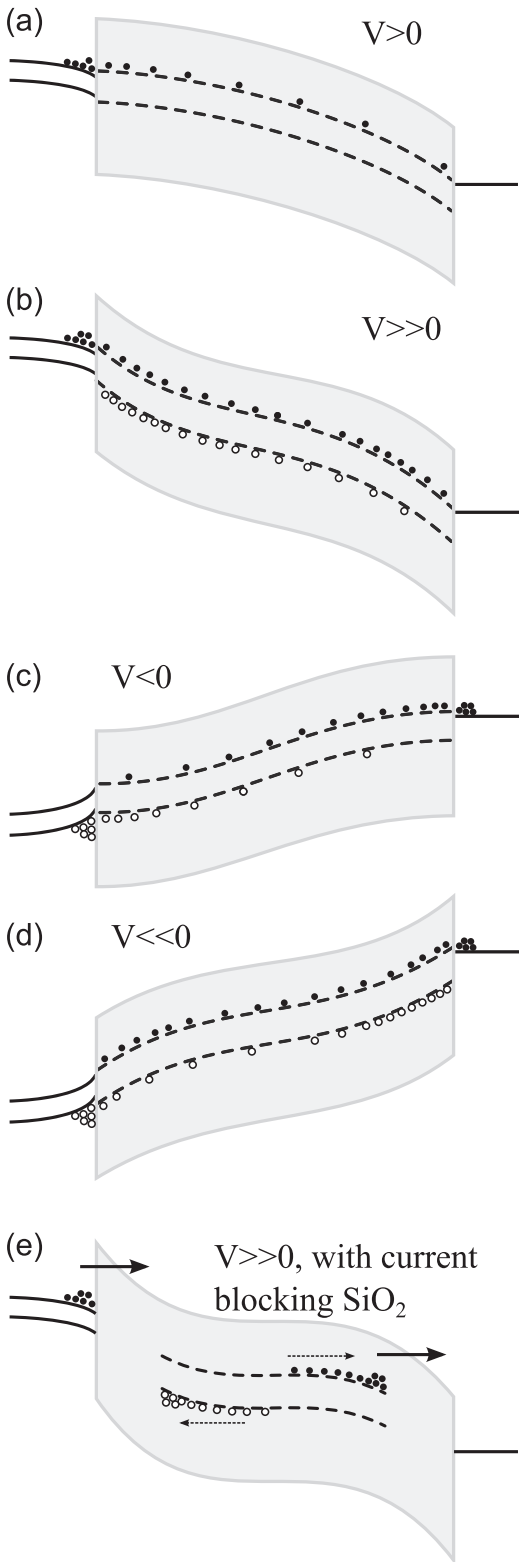

FIG. 6. Schematic of charge flow for the different bias regions applied to Si/SiO_2 SL. (a) Low positive bias, the current becomes limited by the space-charge from injected electrons at the substrate; (b) high positive bias, electron-hole pairs are created and separated and diffuse to the respective contacts; (c) low negative bias under illumination, holes and electrons are injected at the silicon interface and metal interface, respectively; (d) high negative bias, the additional charge separation process is superimposed on the carrier injection process; (e) the case for samples H3 and H4: Holes are pushed towards the silicon substrate, whereas electrons are pushed towards the aluminum gate, due to the large tunneling barrier, the carriers remain trapped in the SL, but Fowler-Nordheim injection from the silicon substrate becomes possible.

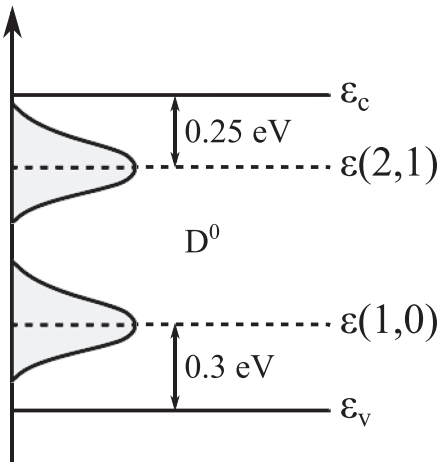

FIG. 7. Energy representation of the Si surface DB, $\varepsilon(1,0)$ and $\varepsilon(2,1)$ denote the charge transition levels, ε_C and ε_V are the Si conduction and valence band edges, respectively.

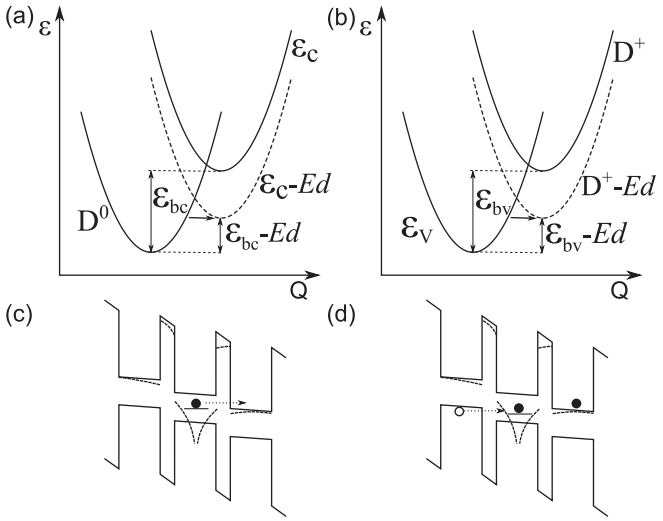

FIG. 8. (a) and (b) represent configuration coordinate diagrams for the electric field enhanced transitions from (a) a DB state to the ground conduction state of a SiNC and (b) tunneling of a valence band electron to a charged defect state D^+, (c) energy band diagram representation of the transition in (a), (d) energy band diagram representation of the transition in (b). The dashed lines in (c) and (d) indicate the positive defect coulomb potential that is seen by the defect electron in (c) and by the valence electrons in case of the charged D^+ state in (d).

flatband shift just measures a net charge, a more detailed optoelectronic characterization seems to be desirable. However, this is beyond the scope of the present work.

B. The role of Si surface states

Hydrogen passivation is well known to reduce the density of Si surface dangling bonds (DB) at the $SiNC/SiO_2$ interface[51–53] usually leading to superior photoluminescence properties.[9,54–57] Hence, the effect of hydrogen passivation is investigated in this work in order to reveal the possible influence of Si DBs on the transport and the charge separation mechanism. The clear dependence on hydrogen passivation reported in Fig. 5 suggests that the transport and charging properties are inherently linked to the presence of Si surface DBs. As a consequence Si DBs are identified to play the major role in the observed charge separation process. Electron spin resonance studies on similar samples as investigated here have indicated that a significant amount of Si DBs exists on the surface of the SiNCs even after hydrogen passivation.[10,11,58] The influence of Si DBs on charge transport has received little attention in the past, but it has been shown by means of electrically detected magnetic resonance that Si surface DBs influence the electronic transport even for large-diameter SiNC ensembles.[59] One may expect that the influence increases drastically as the SiNCs become smaller due to the enhanced surface to volume ratio. As we will show in the following, our electrical measurements can be well explained qualitatively by assuming charge transport and separation that takes place via the Si/SiO_2 surface states. The paramagnetic Si surface DB (i.e., the P_b defect) is energetically centered between the Si conduction and valence band and is occupied by one electron in the neutral case. The amphoteric nature of the P_b center allows for three distinct charge states within the Si bandgap. In the bulk interface case, the $\varepsilon(2,1)$ charge transition level is located at 0.25 eV below the conduction band, whereas the $\varepsilon(1,0)$ charge transition level is located at 0.3 eV above the valence band.[60–62] The corresponding situation is summarized in Fig. 7. Moreover, it has been shown theoretically that the charge transition levels should closely follow the band edge shifts imposed by quantum confinement.[38] One can imagine that under the application of an electric field, the neutral DB is ionized by the tunneling of the electron to the conduction band of an adjacent SiNC in the framework of the Poole-Frenkel effect. Such a transition from a deep defect level is routinely described by the use of a configuration coordinate diagram.[63,64] In Fig. 8(a), we plot the system energy as a function of the dimensionless lattice coordinate Q for the neutral DB and the lowest conduction state of a neighboring SiNC. By interaction with the lattice, the electron can increase its energy along the parabola. A tunneling transition to the SiNC conduction state can only occur, if the electron gains enough energy to overcome the energy barrier ε_{bc}. Since this barrier is usually too large, the application of an electric field can reduce its magnitude significantly as shown by the dashed line in Fig. 8(a). The rate of the electric field-assisted nuclear tunneling transition of a deep defect state to the conduction band was treated theoretically[65–67] and has been shown to increase as $\propto \exp(aE^2)$, i.e., it could well explain the strong electric field dependence of the current density observed here. In our case, this tunneling rate is modified by the transmission probability that crucially depends on the distance d and structure between the donor and the acceptor states. The corresponding transition is highlighted in the band diagram representation of Fig. 8(c). Once this transition has occurred, the DB relaxes to the D^+ charge state by the emission of multiple phonons. This new situation should allow for a second transition between electrons in the valence band and the charged DB. The configuration coordinate diagram and band diagram is presented in Figs. 8(b) and 8(d), respectively. In this way, a space-separated free electron-hole pair is created by the presence of the defect. Please note that the positively ionized defect potential leads to barrier height

decrease as indicated in Figs. 8(c) and 8(d). The carriers can then diffuse to the respective contacts by direct tunneling between adjacent SiNCs and may explain the charge separation observed in this work by means of C-V flatband shifts. In order to justify the proposed mechanism even for the well passivated samples, we estimate the volume density of DBs. In our previous work, we measured a DB density after hydrogen passivation of around $2 \times 10^{11}\,\mathrm{cm}^{-2}$ per effective Si/SiO_2 interface area, almost independent of SiNC size.[11] Assuming a similar areal SiNC density of $2 \times 10^{12}\,\mathrm{cm}^{-2}$ for the samples studied here,[10] a volume density of around 1×10^{17} DB cm^{-3} is derived which is of the same order of magnitude as the measured trapped charges. Turning back to Fig. 5(a), we can relate the tremendous current decrease after hydrogen passivation with a decrease in DBs over the whole studied electric field range. The extent of the current decrease is on the order of magnitude that is usually seen for the hydrogen DB passivation efficiency. In fact, the proposed mechanism can be understood as defect-assisted band-to-band tunneling mechanism that appears to be more likely than a pure band-to-band tunneling. The energy barrier for tunneling is approximately halved and clear correlation exists with the existence of Si DBs.

V. CONCLUSION

We have studied in detail the charge transport behavior of a large variety of SL samples by I-V and C-V measurements. We demonstrated by TEM that a decrease of the SiO_2 barrier thickness down to 1 nm is possible without a significant loss of the SL structure in case of the used PECVD process. Space-charge-limited current can be observed for a high number of bilayers. However, the underlying transport mechanism cannot be ascribed to any of the well-known expressions for charge transport in dielectrics. In contrast, we found that Si surface dangling bonds are involved in the charge transport in a beneficial way to the extent that charge separation occurs via a two-step defect-assisted band-to-band transition at moderate electric fields. In light of these results, it is important to note that the presence of defects is detrimental for solar cell devices as the exciton lifetime is decreased.

ACKNOWLEDGMENTS

This work was financially supported by German Research Foundation (ZA191/24-1, ZA191/27-1). The research leading to these results has received funding from the European Community's Seventh Framework Programme (FP7/2007-2013) under Grant Agreement No. 245977.

[1]L. T. Canham, Appl. Phys. Lett. **57**, 1046 (1990).
[2]V. Lehmann and U. Gösele, Appl. Phys. Lett. **58**, 856 (1991).
[3]G. Franzo, A. Irrera, E. C. Moreira, M. Miritello, F. Iacona, D. Sanfilippo, G. D. Stefano, P. G. Fallica, and F. Priolo, Appl. Phys. A **74**, 1 (2002).
[4]R. J. Walters, G. I. Bourianoff, and H. A. Atwater, Nature Mater. **4**, 143 (2005).
[5]L. Pavesi, L. D. Negro, C. Mazzoleni, G. Franzo, and F. Priolo, Nature **408**, 440 (2000).
[6]J. Ruan, P. M. Fauchet, L. D. Negro, M. Cazzanelli, and L. Pavesi, Appl. Phys. Lett. **83**, 5479 (2003).
[7]G. Conibeer, M. Green, R. Corkish, Y. Cho, E.-C. Cho, C.-W. Jiang, T. Fangsuwannarak, E. Pink, Y. Huang, T. Puzzer, T. Trupke, B. Richards, A. Shalav, and K.-L. Lin, Thin Solid Films **511–512**, 654 (2006).
[8]M. Zacharias, J. Heitmann, R. Scholz, U. Kahler, M. Schmidt, and J. Bläsing, Appl. Phys. Lett. **80**, 661 (2002).
[9]A. M. Hartel, S. Gutsch, D. Hiller, and M. Zacharias, Phys. Rev. B **85**, 165306 (2012).
[10]D. Hiller, M. Jivanescu, A. Stesmans, and M. Zacharias, J. Appl. Phys. **107**, 084309 (2010).
[11]M. Jivanescu, D. Hiller, M. Zacharias, and A. Stesmans, Europhys. Lett. **96**, 27003 (2011).
[12]J.-W. Luo, P. Stradins, and A. Zunger, Energy Environ. Sci. **4**, 2546 (2011).
[13]K. Seino, F. Bechstedt, and P. Kroll, Phys. Rev. B **86**, 075312 (2012).
[14]C.-W. Jiang and M. A. Green, J. Appl. Phys. **99**, 114902 (2006).
[15]P. Löper, R. Müller, D. Hiller, T. Barthel, E. Malguth, S. Janz, J. C. Goldschmidt, M. Hermle, and M. Zacharias, Phys. Rev. B **84**, 195317 (2011).
[16]I. Balberg, J. Appl. Phys. **110**, 061301 (2011).
[17]I. Perez-Wurfl, X. Hao, A. Gentle, D.-H. Kim, G. Conibeer, and M. A. Green, Appl. Phys. Lett. **95**, 153506 (2009).
[18]A. Marconi, A. Anopchenko, M. Wang, G. Pucker, P. Bellutti, and L. Pavesi, Appl. Phys. Lett. **94**, 221110 (2009).
[19]R. Rölver, B. Berghoff, D. Bätzner, B. Spangenberg, H. Kurz, M. Schmidt, and B. Stegemann, Thin Solid Films **516**, 6763 (2008).
[20]A. M. Hartel, D. Hiller, S. Gutsch, P. Löper, S. Estradé, F. Peiró, B. Garrido, and M. Zacharias, Thin Solid Films **520**, 121 (2011).
[21]G. B. Assayag, C. Bonafos, M. Carrada, A. Claverie, P. Normand, and D. Tsoukalas, Appl. Phys. Lett. **82**, 200 (2003).
[22]A. K. Jonscher, Nature **267**, 673 (1977).
[23]H. Reisinger, G. Steinlesberger, S. Jakschik, M. Gutsche, T. Hecht, M. Leonhard, U. Schröder, H. Seidl, and D. Schwann, in *Digest of IEEE International Electron Device Meeting 01* 12.2.1 (2001).
[24]E. R. v. Schweidler, Ann. Phys. **329**, 711 (1907).
[25]D. K. Schroder, *Semiconductor Material and Device Characterization*, 3rd ed. (Wiley, 2006).
[26]E. H. Nicollian and J. R. Brews, *MOS Physics and Technology* (Wiley, 1982).
[27]A. M. Hartel, S. Gutsch, D. Hiller, C. Kübel, N. Zakharov, P. Werner, and M. Zacharias, Appl. Phys. Lett. **101**, 193103 (2012).
[28]W. Shockley, J. Appl. Phys. **9**, 635 (1938).
[29]S. Ramo, Proc. IRE **27**, 584 (1939).
[30]M. D. Sirkis and N. Holonyak, Am. J. Phys. **34**, 943 (1966).
[31]A. Anopchenko, A. Marconi, E. Moser, S. Prezioso, M. Wang, L. Pavesi, G. Pucker, and P. Bellutti, J. Appl. Phys. **106**, 033104 (2009).
[32]A. Miller and E. Abrahams, Phys. Rev. **120**, 745 (1960).
[33]J. Cai and C.-T. Sah, J. Appl. Phys. **89**, 2272 (2001).
[34]S. Datta, Superlattices Microstruct. **28**, 253 (2000).
[35]S. Datta, *Quantum Transport: Atom to Transistor* (Cambridge University Press, 2005).
[36]J. Bardeen, Phys. Rev. Lett. **6**, 57 (1961).
[37]A. D. Gottlieb and L. Wesoloski, Nanotechnology **17**, R57 (2006).
[38]C. Delerue and M. Lannoo, *Nanostructures: Theory and Modelling* (Springer, 2004).
[39]T. Creazzo, B. Redding, E. Marchena, J. Murakowski, and D. W. Prather, J. Lumin. **130**, 631 (2010).
[40]A. Irrera, F. Iacona, I. Crupi, C. D. Presti, G. Franzo, C. Bongiorno, D. Sanfilippo, G. D. Stefano, A. Piana, P. G. Fallica, A. Canino, and F. Priolo, Nanotechnology **17**, 1428 (2006).
[41]S. Prezioso, A. Anopchenko, Z. Gaburro, L. Pavesi, G. Pucker, L. Vanzetti, and P. Bellutti, J. Appl. Phys. **104**, 063103 (2008).
[42]X. D. Pi, O. H. Y. Zalloum, A. P. Knights, P. Mascher, and P. J. Simpson, J. Phys.: Condens. Matter **18**, 9943 (2006).
[43]M. A. Rafiq, Z. A. K. Durrani, H. Mizuta, M. M. Hassan, and S. Oda, J. Appl. Phys. **104**, 123710 (2008).
[44]J. Frenkel, Phys. Rev. **54**, 647 (1938).
[45]T. A. Burr, A. A. Seraphin, E. Werwa, and K. D. Kolenbrander, Phys. Rev. B **56**, 4818 (1997).
[46]M. A. Rafiq, Y. Tsuchiya, H. Mizuta, S. Oda, S. Uno, Z. A. K. Durrani, and W. I. Milne, Appl. Phys. Lett. **87**, 182101 (2005).
[47]A. Rose, Phys. Rev. **97**, 1538 (1955).
[48]P. Mark and W. Helfrich, J. Appl. Phys. **33**, 205 (1962).
[49]I. Crupi, S. Lombardo, E. Rimini, B. F. C. Gerardi, and M. Melanotte, Appl. Phys. Lett. **81**, 3591 (2002).

[50]V. I. Turchanikov, A. N. Nazarov, V. S. Lysenko, J. Carreras, and B. Garrido, J. Phys.: Conf. Ser. **10**, 409 (2005).
[51]S. Godefroo, M. Hayne, M. Jivanescu, A. Stesmans, M. Zacharias, O. I. Lebedev, G. van Tendeloo, and V. V. Moshchalkov, Nat. Nanotechnol. **3**, 174 (2008).
[52]M. Jivanescu, A. Stesmans, and M. Zacharias, J. Appl. Phys. **104**, 103518 (2008).
[53]A. Stesmans, M. Jivanescu, S. Godefroo, and M. Zacharias, Appl. Phys. Lett. **93**, 023123 (2008).
[54]S. Cheylan and R. G. Elliman, Appl. Phys. Lett. **78**, 1225 (2001).
[55]A. R. Wilkinson and R. G. Elliman, J. Appl. Phys. **96**, 4018 (2004).
[56]A. M. Hartel, S. Gutsch, D. Hiller, and M. Zacharias, Phys. Rev. B **87**, 035428 (2013).
[57]S. Gutsch, A. M. Hartel, D. Hiller, N. Zakharov, P. Werner, and M. Zacharias, Appl. Phys. Lett. **100**, 233115 (2012).
[58]D. Hiller, S. Goetze, F. Munnik, M. Jivanescu, J. W. Gerlach, J. Vogt, E. Pippel, N. Zakharov, A. Stesmans, and M. Zacharias, Phys. Rev. B **82**, 195401 (2010).
[59]A. R. Stegner, R. N. Pereira, K. Klein, R. Lechner, R. Dietmueller, M. S. Brandt, M. Stutzmann, and H. Wiggers, Phys. Rev. Lett. **100**, 026803 (2008).
[60]N. M. Johnson, D. K. Biegelsen, M. D. Moyer, S. T. Chang, E. H. Poindexter, and P. J. Caplan, Appl. Phys. Lett. **43**, 563 (1983).
[61]M. Lannoo, C. Delerue, and G. Allan, J. Lumin. **70**, 170 (1996).
[62]M. Lannoo, C. Delerue, and G. Allan, J. Lumin. **57**, 243 (1993).
[63]C. H. Henry and D. V. Lang, Phys. Rev. B **15**, 989 (1977).
[64]B. K. Ridley, J. Phys. C **11**, 2323 (1978).
[65]V. Karpus and V. I. Perel, JETP Lett. **42**, 497 (1985).
[66]S. Makram-Ebeid and M. Lannoo, Phys. Rev. B **25**, 6406 (1982).
[67]V. Karpus and V. I. Perel, Sov. Phys. JETP **64**, 1376 (1986).